

# Charge Carrier Lifetime Fluctuations and Performance Evaluation of Cu(In,Ga)Se<sub>2</sub> Absorbers via Time-Resolved-Photoluminescence Microscopy

Mario Ochoa,\* Shih-Chi Yang, Shiro Nishiwaki, Ayodhya N. Tiwari, and Romain Carron\*

The open-circuit voltage ( $V_{OC}$ ) is the main limitation to higher efficiencies of Cu(In,Ga)Se<sub>2</sub> solar cells. One of the most critical parameters directly affecting  $V_{OC}$  is the charge carrier lifetime. Therefore, it is essential to evaluate the extent to which inhomogeneities in material properties limit the carrier lifetime and how postdeposition treatments (PDTs) and growth conditions affect material properties. Time-resolved photoluminescence (TRPL) microscopy is employed at conditions similar to one sun to study carrier lifetime fluctuations in Cu(In,Ga)Se<sub>2</sub> with light (Na) and heavy (Rb) alkalis, different substrates, and grown at different temperatures. PDT lowers the amplitude of minority carrier lifetime fluctuations, especially for Rb-treated samples. Upon PDT, the grains' carrier lifetime increases, and the analysis suggests a reduction in grain boundary recombination. Furthermore, lifetime fluctuations have a small impact on device performance, whereas  $V_{OC}$  calculated from TRPL (and continuous-wave PL) agrees with device values within the limits of investigated PDT samples. Finally, up to about half a per cent external radiative efficiencies are experimentally determined from TRPL metrics, and internal radiative efficiencies are approximated. The findings demonstrate that the highest absorber material quality investigated is still limited by nonradiative recombination (grain or grain boundary) and is comparable to state-of-the-art absorbers.

occur at the sub-micrometer or micrometer level. Hence, several microscopic and imaging techniques have been applied to study GBs, lateral inhomogeneities and overall performance.<sup>[1–9]</sup> For instance, positive potential barriers at GBs were suggested using electron beam-induced current (EBIC) measurements.<sup>[10]</sup> These barriers inhibited increased recombination at twin boundaries. A negative role of potential fluctuations at the GBs was suggested from cathodoluminescence studies.<sup>[8,11]</sup> Correlative measurements including EBIC, electron backscattered diffraction, and atomic probe tomography showed the composition of GBs, and the presence of Na and oxygen determine its nature, i.e., beneficial, detrimental or neutral.<sup>[12]</sup> Cu-rich and Cu-poor GBs have also been suggested.<sup>[12,13]</sup> Recently, technology computer-aided design (TCAD) simulations implementing realistic grain structure, net doping, and charge carrier lifetime fluctuations, have shown their limited influence on device performance.<sup>[11]</sup> On the contrary, GBs recom-

## 1. Introduction


Lateral nonuniformities in chemical composition, structural defects, and even structural voids can be found in polycrystalline Cu(In,Ga)Se<sub>2</sub> (CIGS) solar cells. These lateral variations give rise to changes in material properties such as potential fluctuations, localized band bending, net doping, and carrier recombination within the grains and at the grain boundaries (GBs), among others. Such changes in material properties often

combination velocities determined from cathodoluminescence suggested they could limit the open-circuit voltage ( $V_{OC}$ ) depending on their nature.<sup>[11]</sup> On the macroscopic level, effective detection of shunts and a correlation of photoluminescence (PL) and electroluminescence to device performance have been reported.<sup>[14]</sup> Overall, it is still debated to what extent GBs and material properties inhomogeneities limit the  $V_{OC}$ .

It is essential to evaluate the carrier lifetime inhomogeneities to identify  $V_{OC}$  limiting factors. The carrier lifetime is one of the most critical parameters directly affecting  $V_{OC}$ , thus device performance. In micrometer-scale, time-resolved photoluminescence (TRPL) microscopy can be used to measure the carrier lifetime directly. Compared to steady-state PL, the carrier lifetime is less sensitive to sample topography, which could mask its actual value. Besides, if proper conditions are met, TRPL is an excellent technique for material quality prediction providing insight into the charge carrier dynamics. Interpretation is usually challenging; however, a careful analysis could provide valuable information regarding other material parameters, e.g., doping concentration, surface recombination, charge carrier extraction, among others.

TRPL microscopy using two-photon excitation (2PE) has demonstrated high resolution under low injection conditions

M. Ochoa, S.-C. Yang, S. Nishiwaki, A. N. Tiwari, R. Carron  
Laboratory for Thin Films and Photovoltaics  
Empa-Swiss Federal Laboratories for Materials Science and Technology  
Ueberlandstrasse 129, Dübendorf CH-8600, Switzerland  
E-mail: Mario.ochoa@empa.ch; Romain.carron@empa.ch

 The ORCID identification number(s) for the author(s) of this article can be found under <https://doi.org/10.1002/aenm.202102800>.

© 2021 The Authors. Advanced Energy Materials published by Wiley-VCH GmbH. This is an open access article under the terms of the Creative Commons Attribution License, which permits use, distribution and reproduction in any medium, provided the original work is properly cited.

DOI: 10.1002/aenm.202102800

characterizing the bulk lifetime, surface and grain boundary recombination, and transport properties for materials other than CIGS.<sup>[15,16]</sup> Due to the low absorption probability of the two-photon absorption process, high laser power is required. Typically, to achieve the high photon density needed, 2PE microscopy uses not easily accessible femtosecond lasers and diffraction-limited beam sizes. In such cases, recombination and lateral carrier diffusion out of the collection volume play a key role in the decays. Other systems, more accessible, implement one-photon excitation.<sup>[17]</sup> However, for diffraction-limited beam sizes (i.e., confocal mode), it is extremely challenging to achieve high optical resolution and remain in low injection for CIGS. A different—and complementary—approach is the use of wide-field (or uniform) illumination. Expanding the illumination area reduces the photon density, and low injection is simpler to accomplish. Besides, wide-field illumination avoids the lateral carrier out-diffusion problem, being more representative of the standard illumination conditions of solar cells. The main challenge is to achieve low injection conditions and high optical resolution due to the high detection sensitivity required and the relatively small size of the grains, i.e., between some hundreds of nm up to a few micrometers.

This work uses TRPL mapping under wide-field illumination to study the microscopic charge carrier dynamics of several CIGS absorbers grown at different temperatures, substrates, and with different post-deposition treatments (PDT). A comparison with continuous-wave PL (PL-CW) mapping is performed, and the implications of the measurement conditions are discussed along with the paper assisted by power-dependent measurements and numerical simulations. We also present the experimental determination of external radiative efficiency from TRPL parameters and a voltage loss analysis of state-of-the-art CIGS solar cells from the measurements at low injection.

## 2. Results and Discussion

The five samples investigated include double-graded absorbers grown on soda-lime glass (SLG) and stainless-steel (Steel) at low temperature (LT) and high temperature (HT) with different PDT applied: No PDT, NaF, and NaF + RbF (see the Experimental Section for more details about the samples). For TRPL mapping, solar cells of layer structure CdS/CIGS/Mo were used after etching away ZnO layers to access the same region where conventional photovoltaic (PV) characterization was performed. As previously shown by Metzger et al.<sup>[18]</sup> and suggested by Weiss et al.,<sup>[19]</sup> the presence of CdS has a minor or null impact on the TRPL decay, which applies to the samples studied here. The solar cells investigated exhibit a significant difference in performance, as shown by the *I*–*V* parameters of Table 1.

### 2.1. TRPL Mapping under Wide-Field Illumination

This section discusses spatial variations exhibited by the TRPL maps, whereas the relative comparison between TRPL parameters quantities and distributions linked to device performance will be shown in Section 2.4.

**Table 1.** *I*–*V* parameters of solar cells with different PDT processes, substrate, and growth temperature. No ARC has been deposited onto the solar cells.

Solar cell	$J_{sc}$ [mA cm <sup>-2</sup> ]	$V_{oc}$ [mV]	FF [%]	Efficiency [%]
NaF + RbF Steel (HT)	37.3	700	73.0	19.1
NaF + RbF SLG (HT)	35.3	742	77.2	20.2
NaF + RbF SLG (LT)	35.9	735	76.9	20.3
NaF SLG (LT)	34.7	686	74.0	17.6
No PDT SLG (LT)	33.0	569	65.0	12.2

Figure 1 shows a set of maps of TRPL parameters (*A*,  $\tau$ , and  $A \times \tau$ ), and steady-state PL (labeled PL-CW) for the samples. At each pixel, we fitted the decay with a single exponential  $A \cdot e^{-t/\tau}$  function (see the Experimental Section) where *A* is the intensity at time *t* = 0, and  $\tau$  is the carrier lifetime.  $A \times \tau$  is a good approximation of total PL emission and can be directly linked to PL quantum yield, a good material quality indicator (see Section 2.4). Besides,  $A \times \tau$  maps highlight which parameter (*A* or  $\tau$ ) dominates the fluctuations. Full decays are shown in Figure S1 of the Supporting Information, exhibiting well-behaved transients with no initial dip.  $\tau$  maps show slight variations for PDT samples, and higher fluctuations are observed for No PDT sample. The other parameters (*A*,  $A \times \tau$ , and PL-CW) show similar fluctuations with also higher variations for the no PDT case. For PDT samples, these fluctuations can be due to topography variations, morphology, bandgap fluctuations, or even the presence of voids. Under low injection, *A* (at *t* = 0) can be linked to the doping concentration of the material, and slight fluctuations in doping density will also directly affect this parameter. For no PDT samples, the fluctuations in *A*,  $A \times \tau$ , and PL-CW are higher than PDT samples and similar to lifetime fluctuations indicating all TRPL parameters capture variations in material quality.

A quantitative analysis of TRPL parameters fluctuations and correlations is shown in Figure 2. To measure the amount of data dispersion, we use the deviation from the mean value:

$$\sigma_{\text{mean},x} = 100 \times \frac{x_i - x_{\text{mean}}}{x_{\text{mean}}}, \text{ where } x \text{ represent a given TRPL}$$

or PL-CW parameter shown in Figure 1,  $x_i$  the pixel data and  $x_{\text{mean}}$  the mean value of the full map for the corresponding (TR)PL parameter. 2D histograms of mean value deviations are depicted for two parameter pairs: (a) *A* and  $\tau$ , and (b)  $A \times \tau$  and PL-CW.

The former (a) provides the degree of variation of the TRPL parameters within each sample. The deviations are small, between  $\pm 20\%$  for PDT samples and larger for No PDT, but remain moderate up to  $\pm 40\%$ . The Pearson correlation coefficient (PCC) can quantify the degree of correlation between two variables, which ranges between  $-1$  and  $1$  ( $-1$ ,  $0$ , and  $1$  correspond to anticorrelated, uncorrelated, and correlated maps, respectively). Only the No PDT sample exhibits a positive correlation between *A* and  $\tau$  with PCC = 0.46, whereas PDT samples show some degree of anticorrelation. The strongest anticorrelation is exhibited by the NaF + RbF (LT) sample. Anticorrelation means lifetime fluctuations are not dominated by topography. Instead, they are dominated by slight nonuniformity (in recombination or material properties) and/or grain boundary

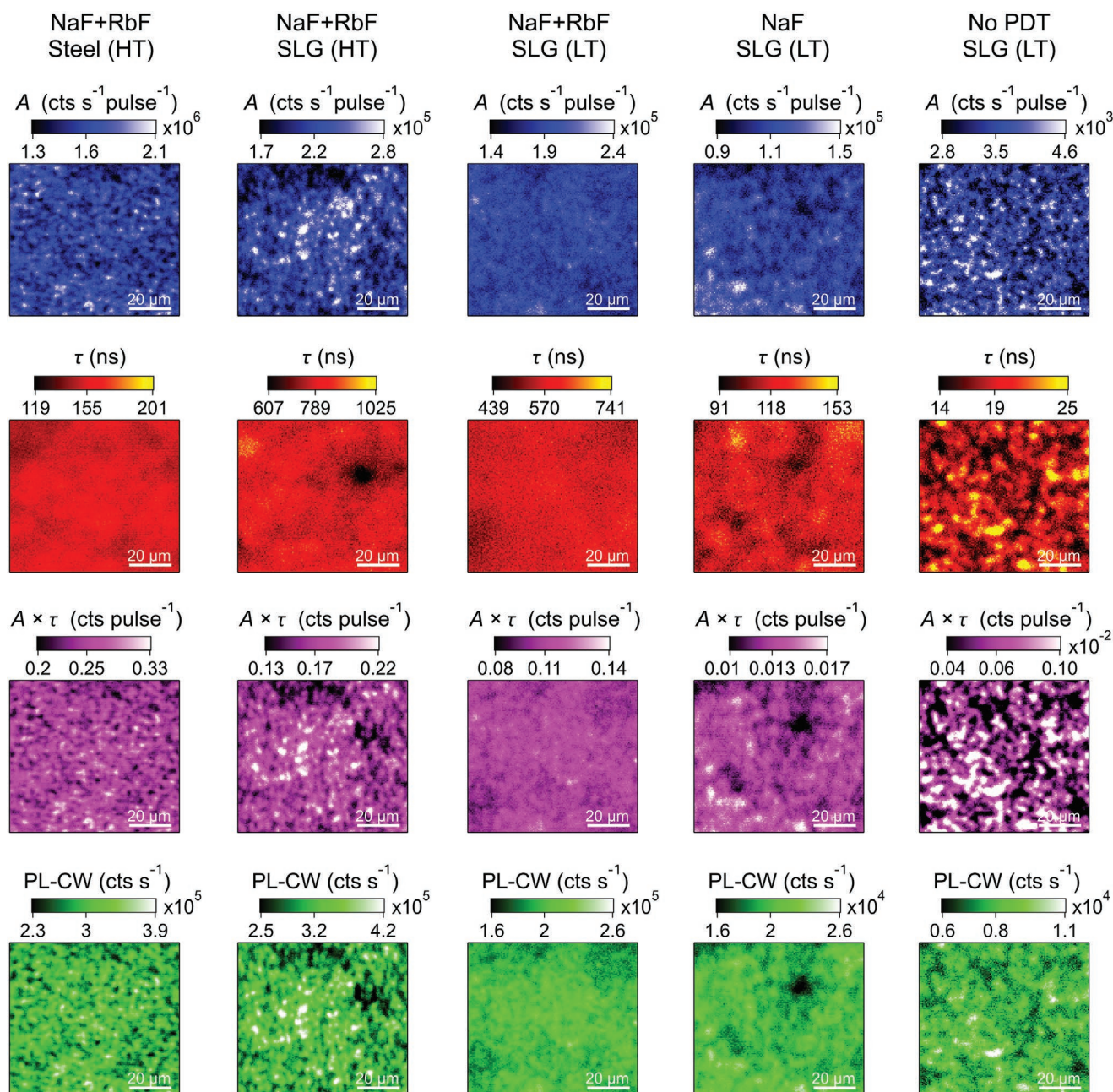


**Figure 1.** Front view maps of TRPL parameters and steady-state PL (PL-CW intensity) of the five samples analyzed. The middle tick of each color scale corresponds to the mean value of the map. The same dynamic range (mean value  $\pm 30\%$ ) was used to set the color scales. The No-PDT PL-CW was measured under higher excitation (seven times) to obtain a reasonably good signal-to-noise ratio. It is still possible to compare it with TRPL at low injection because TRPL maps at comparable power exhibit very similar standard deviations. The standard deviation shows no significant dependence with excitation power (up to seven times higher excitation, not shown) regarding the standard deviation.

recombination. Hence, this highlights one advantage of measuring the carrier lifetime because the decays are significantly less sensitive to small variations in material properties influencing PL or  $A$  maps, which are likely, not relevant for device performance.

TRPL and PL-CW figures of merit are strongly correlated for all samples with  $\text{PCC} > 0.75$  (Figure 2b). Interestingly, the PL-CW and TRPL metrics distribution cannot be considered equivalent for No PDT and NaF samples. For instance, for No PDT sample, the dispersion of  $A \times \tau$  exhibits deviations up to  $\pm 40\%$ .

By contrast, the PL-CW deviation remains within  $\pm 20\%$  (as exemplified by the deviation of the dataset from the dashed line). This result reveals that, for cases in which inhomogeneities are relatively large (e.g., No PDT and, to a lower extent NaF sample), TRPL could detect higher dispersion than PL-CW.

The larger spatial variations exhibited by the No PDT can be attributed to the absence of passivation effect from PDTs at the GBs and within the grains. However, under wide-field illumination, it is known that excess carriers diffuse after some time and redistribute within the volume. To what extent these carriers



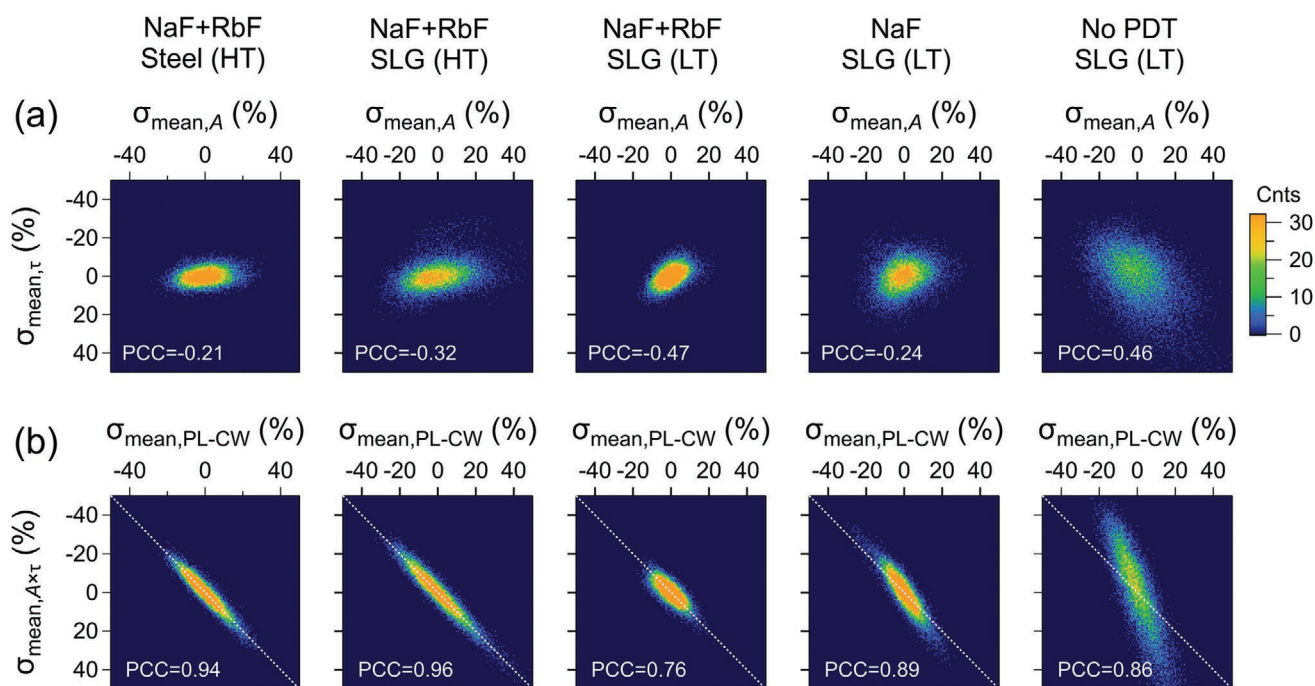


**Figure 2.** 2D histograms of mean deviation for different parameter pairs, i.e., a)  $A$  and  $\tau$  and b) integrated PL-CW and  $A \times \tau$  pair for all samples analyzed. PCC stands for Pearson correlation coefficient (PCC) and indicates the degree of correlation between parameters. In (b), dashed lines illustrate deviations from equality between each parameter distribution.

balance recombination rates and PL spatial inhomogeneities depends on the carrier diffusion length.<sup>[20]</sup> We have previously characterized the lateral diffusion length ( $L_D$ ) of PDT samples ranging from 2 to 9  $\mu\text{m}$ .<sup>[11,21]</sup> The value for No PDT absorbers could not be characterized due to pronounced inhomogeneities. Overall, it is reasonable to expect that nonuniformities in carrier lifetime of No PDT absorber are more visible because its diffusion length is significantly lower than the PDT counterparts. However, this is not the case. By comparing, for example, the Steel and No PDT samples, Steel sample exhibits  $L_D$  in the range of the optical resolution of the system (2 to 3  $\mu\text{m}$ ),<sup>[21]</sup> and it is reasonable to expect lower  $L_D$  for No PDT sample. Hence, the impact of carrier diffusion on the lifetime inhomogeneities is minimum for both samples. As shown in the lifetime maps of Steel and No PDT samples in Figure 1, it is evident that material quality homogeneity enhances upon PDT. This enhancement agrees with the  $\tau$  standard deviations, being 3.3%, 4.3%, 5.6%, 6.5%, and 11.8% for Steel, NaF + RbF (LT), NaF + RbF (HT), NaF (LT), and No PDT (LT) samples, respectively.

## 2.2. Grain Boundary Recombination

In the maps shown in Figure 1, it is not possible to directly distinguish GB recombination and nonuniformity. This distinction determines if grain interior or GB recombination limits the carrier lifetime. In principle, GB recombination locally reduces the PL signal, and its spatial influence depends on the carrier transport properties. Hence, the carrier diffusion length, optical resolution of the system, and conditions (see Figure S2, Supporting Information) influence GB recombination detection.

In this context, we first evaluate the sensitivity of the measurements to GB recombination and then apply an indirect analysis to assess effective GB recombination. To understand the experimental sensitivity to GB recombination, we model a simple 2D structure with two CIGS regions of 1  $\mu\text{m}$  thickness (emulating two columnar grains) and setting an interface boundary condition with variable effective GB recombination velocity ( $S_{GB}$ ). The inset of Figure 3a depicts the model structure used for simulations. We simulate the PL transients after pulsed illumination and spatially integrate the time-dependent radiative recombination only along a columnar region centered at the GB (referred to as  $\text{PL}_{GB}$ ).  $\text{PL}_{GB}$  resembles the light collection area in the experimental configuration and its length is set to 0.5 and 2  $\mu\text{m}$  (in the range of the optical resolution of the system). Figure 3a shows the ratio of  $\text{PL}_{GB}$  as compared to a reference

$$\text{case with } S_{GB} = 0 \text{ cm s}^{-1}, \text{ i.e., } \text{PL}_{GB, \text{ratio}}(S_{GB}) = \frac{\text{PL}_{GB}(S_{GB})}{\text{PL}_{GB}(S_{GB} = 0)},$$

for five different  $L_D$  representative of all samples. Different  $L_D$  is accomplished by varying the effective carrier lifetimes ( $\tau_{\text{eff}}$ , shown as tags on the curves in ns) and fixed carrier mobility (40  $\text{cm}^2 \text{V}^{-1} \text{s}^{-1}$ ).<sup>[21]</sup>  $\text{PL}_{GB, \text{ratio}}$  represents the fraction of carriers recombined at the GB within the optical resolution (2  $\mu\text{m}$ , solid lines) and for an illustrative case in which the optical resolution of the system is hypothetically enhanced four times (500 nm, dashed lines).

Longer lifetimes cases have larger sensitivity to  $S_{GB}$ . For instance, for  $S_{GB} \approx 600 \text{ cm s}^{-1}$  and  $\tau_{\text{eff}} = 800 \text{ ns}$ ,  $\text{PL}_{GB, \text{ratio}}$  is 80%, and for  $\tau_{\text{eff}} = 15 \text{ ns}$ ,  $\text{PL}_{GB, \text{ratio}}$  is only 2.5%. Therefore, GB recombination influence is smaller for lower  $\tau_{\text{eff}}$  (15 ns) and larger sensitivity to GB recombination is mainly expected for

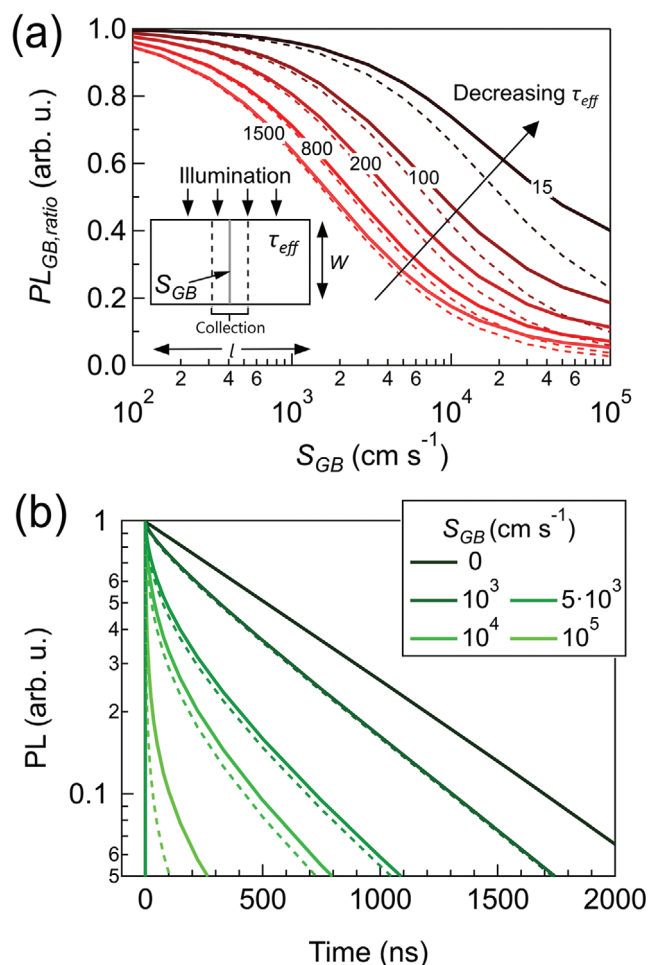


**Figure 3.** a) Normalized PL variation at the GB as a function of GB recombination velocity ( $PL_{GB,ratio}$ ) for several  $\tau_{eff}$  shown with a tag on each curve (values in ns) corresponding to diffusion lengths of  $\approx 1$ , 3, 4.5, 9, and 12.5  $\mu m$ . The inset shows the 2D simulated structure with  $l = 200 \mu m$ ,  $W = 1 \mu m$ , and a centered boundary condition varying  $S_{GB}$ . The structure is illuminated by a Gaussian beam centered at the GB with a spot size of 130  $\mu m$  to emulate experimental conditions (not significant changes were found by assuming full uniform illumination over 200  $\mu m$  length). Dashed lines in the inset indicate the region where the PL is integrated, corresponding to  $PL_{GB,ratio}$ . b) Simulated PL decays for several  $S_{GB}$  with  $\tau_{eff} = 800$  ns. The simulated PL signal and decays are integrated (collected) along a columnar region of 2  $\mu m$  length (optical resolution) centered at the GB. Dashed lines correspond to PL collection over a length of 500 nm, assuming hypothetical enhanced optical resolution.

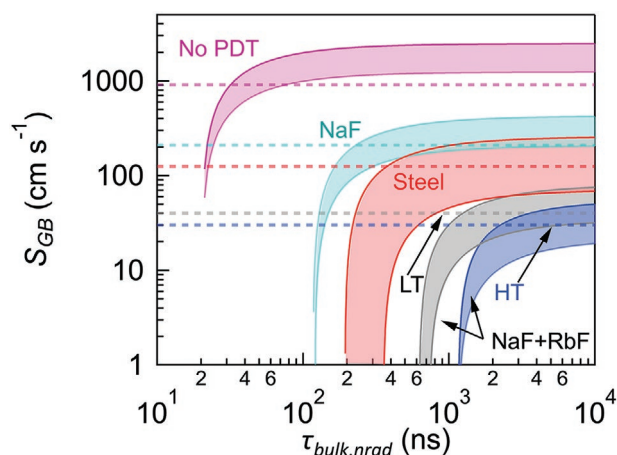
$S_{GB} > 1000 \text{ cm s}^{-1}$ . For our samples ( $\tau_{eff}$  ranges [15 ns, 800 ns] and  $L_D < 10 \mu m$ ), we expect up to 30% PL reduction in the case of a single isolated GB. Hence, the experimental conditions are sensitive to GB recombination for the range of the transport properties of our materials.

Figure 3b shows an example of the simulated decays for  $\tau_{eff} = 800$  ns and several values of  $S_{GB}$  at the location of the GB. GB recombination pronouncedly influences the shape of the decays at initial times. At late times ( $> 500$  ns), the decay slope approaches to the case without GB recombination. At a microscopic level, the recombination at the GB depletes the carriers in its vicinity and causes an initial fast PL decrease. At late

times, the low carrier density induces low recombination, and charge carrier density is determined by diffusion of carriers; therefore, the value tends to  $\tau_{eff}$ . Hence, GB recombination cannot be assessed from the second slope of the decay, being mainly representative of bulk recombination, in agreement with previous literature.<sup>[20,22]</sup> On the contrary, initial times are more influenced by GB recombination.

There are two main difficulties to analyze GB recombination in CIGS absorbers from the initial slope of the decay (characterized by  $\tau_1$ ). First, variable photo generation profiles and nonuniform absorption coefficients ( $\alpha$ ) are present due to graded bandgap and strong absorption in the layer.  $\alpha$  varies  $\approx 10\%$  between the front surface (highest Ga content) and the notch (lowest Ga content). Hence, the use of a direct equation to quantify GB recombination might be compromised, i.e.,  $\tau_1 = \alpha^{-1} S_{GB}^{-1}$ .<sup>[23]</sup> Evaluation of this equation is performed by including it in the following analysis using an average value of  $\alpha$  in the front bandgap grading. This equation considers only GB recombination and surface recombination is neglected. This is reasonable since the bandgap grading has been shown to greatly passivate the back surface,<sup>[24,25]</sup> and to a lower extent, the front surface recombination,<sup>[19]</sup> which is also further passivated by the CdS layer. In any case, the value of  $S_{GB}$  calculated from previous equation can only be considered an upper limit. The second difficulty is related to the fact that GBs exhibit different natures, namely detrimental, neutral, or beneficial.<sup>[9,12]</sup> Often, beneficial GBs exhibit an upward bending of the conduction band, i.e., a barrier for electrons<sup>[9]</sup> (or a valence band-offset, i.e., barrier for holes<sup>[26]</sup>), which could separate the carriers from GBs, artificially reducing the PL signal at initial times. In this scenario, faster decay might not necessarily represent increased GB recombination.

Alternatively, it is possible to determine the upper limits of effective GB recombination by considering recombination rates from different origins are additive, and the total inverse recombination rate yield the carrier lifetime, such that the effective lifetime is given by  $\tau_{eff}^{-1} = \tau_{nr}^{-1} + \tau_{rad}^{-1}$ , being  $\tau_{nr}^{-1} = \tau_{bulk,nrad}^{-1} + \tau_{GB}^{-1}$ . The GB lifetime ( $\tau_{GB}$ ) is dependent on the grain size ( $d$ ) and the effective GB recombination velocity ( $S_{GB}$ ), defined as  $\tau_{GB} = \frac{d}{2S_{GB}}$ .<sup>[27]</sup>  $S_{GB}$  must be considered as effective average values for GB recombination velocities, including an average influence of any GB nature. In this way, we can estimate the upper limit to  $S_{GB}$  and deduce a bulk nonradiative lifetime that complies with the effective values measured. Assuming grain size  $d$  lies between 500 and 1000 nm, and  $\tau_{rad}$  between 250 ns and 3  $\mu s$  (depending on the doping concentration and photon recycling effects), **Figure 4** depicts  $S_{GB}$  for all samples analyzed as a function of the nonradiative bulk lifetime ( $\tau_{bulk,nrad}$ ) using the harmonic mean (solid lines and shaded regions) and  $\tau_1$  (horizontal dashed lines). The maximum values of  $S_{GB}$  are  $\approx 60 \text{ cm s}^{-1}$  for NaF + RbF (HT),  $80 \text{ cm s}^{-1}$  for NaF + RbF (LT),  $250 \text{ cm s}^{-1}$  for Steel,  $400 \text{ cm s}^{-1}$  for NaF, and  $3300 \text{ cm s}^{-1}$  for No PDT. These values suggest PDT not only enhances grain interior lifetime but also reduces GB recombination. Interestingly, the intersection between the values calculated via  $\tau_1$  (horizontal dashed lines) and the harmonic mean (shaded regions) seems consistent and suggests  $\tau_{bulk,nrad}$  about 2  $\mu s$  for NaF + RbF samples. This lifetime value is remarkable and reasonable for such a high material quality, being in the range of radiative lifetime. By



**Figure 4.**  $S_{GB}$  as a function of  $\tau_{bulk,nrad}$  for all samples analyzed considering grain sizes between 500 and 1000 nm and different radiative lifetimes due to different doping for each sample. Dashed lines correspond to  $S_{GB}$  calculated via  $\tau_1 = \alpha^{-1} S_{GB}^{-1}$ ,<sup>[23]</sup> in which  $\tau_1$  is extracted from a fit to the first slope of the decays at each pixel of the maps shown previously. The height of each dashed line corresponds to the standard deviation (<25% deviation from mean).

considering the samples with effective lifetimes of  $\approx 100$ – $150$  ns (NaF and Steel, respectively), the GB recombination velocities (intersection of dashed lines and shaded regions) are consistent with a previous study in which samples with similar effective lifetimes were examined.<sup>[11]</sup>

Even though low  $S_{GB}$  values are suggested for the NaF + RbF PDT samples, GB recombination could be limiting the effective lifetime due to the high quality of the grains. Therefore, it is necessary to enhance the minority carrier lifetime in the

grains and inhibit GB recombination, e.g., by optimizing PDT growth conditions or by increasing the grain size. For instance, silver alloying is a promising route to increase the grain size and keep high material quality.<sup>[28,29]</sup>

### 2.3. TRPL Power Dependence and Injection Conditions

To estimate  $V_{OC}$  from TRPL measurements (next section), it is required to assess that the injection conditions represent typical operating conditions of CIGS solar cells (one sun). Power-dependent carrier lifetime measurements help to evaluate the operating injection regime of a given illumination condition, e.g., for TRPL maps in Figure 1. These measurements are even more important considering the difficulty to achieve low injection conditions with micrometer resolution mapping and the challenging determination of precise values of absorber doping concentration. In this regard, the charge carrier lifetime should remain constant under low injection conditions. This is valid assuming the carrier lifetime is dominated by nonradiative recombination following Shockley–Read–Hall (SRH) statistics with equal single trap characteristics (i.e., energy level, capture cross-section) for both electrons ( $n$ ) and holes ( $p$ ). At high injection in a p-type material, the excess carrier (electron) density ( $\Delta n$ ) exceeds the equilibrium hole concentration ( $p_0$ ), i.e.,  $\Delta n > p_0$ , the carrier lifetime reduces proportionally to  $\Delta n^{-2}$  for bimolecular radiative recombination and to  $\Delta n^{-3}$  according to Auger recombination. Auger recombination only becomes dominant at a very high injection regime, which was not reached in the experiments ( $\Delta n \approx 10^{20} \text{ cm}^{-3}$ ).<sup>[30]</sup> **Figure 5** shows average effective lifetimes as a function of excess carrier density for all samples analyzed. Three modeled curves (dashed lines) are included to exemplify theoretical trends assuming different

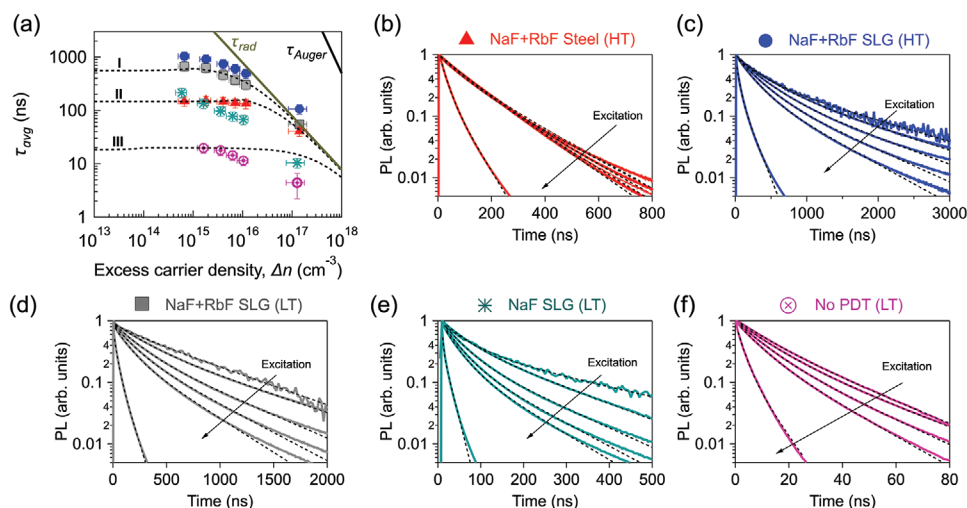


**Figure 5.** a) Average carrier lifetime ( $\tau_{avg}$ ) as a function of excess carrier density for all samples analyzed. Dashed lines correspond to modeled carrier lifetimes for three-parameter sets of doping ( $N_A$ ) and low injection lifetime, respectively: I:  $10^{15} \text{ cm}^{-3}$  and 600 ns, II:  $10^{16} \text{ cm}^{-3}$  and 180 ns, and III:  $10^{14} \text{ cm}^{-3}$  and 18 ns. These three sets of parameters cover the range of experimental lifetime and apparent doping for all samples (see Figure S3, Supporting Information). The radiative lifetime is estimated considering bimolecular radiative coefficient  $B = 1.28 \times 10^{-10} \text{ cm}^3 \text{ s}^{-1}$ . The Auger coefficients for holes and electrons are  $C_p = C_n = 10^{-30} \text{ cm}^6 \text{ s}^{-1}$ , respectively.<sup>[19]</sup> b–f) Experimental TRPL decays (dual-exponential fits are shown in black dashed lines) at the excitation levels shown in (a) integrated over the map area of Figure 1. Experimental TRPL maps shown previously correspond to  $\Delta n < 2 \times 10^{15} \text{ cm}^{-3}$  before bimolecular recombination dominates the overall lifetime. The excess carrier density equivalent to one-sun conditions for lifetimes between 100 and 1000 ns (typical for CIGS) are between  $1.8 \times 10^{14}$  and  $1.8 \times 10^{15} \text{ cm}^{-3}$ , respectively.



carrier lifetimes and doping concentrations (in the range of values according to capacitance–voltage, C–V measurements, see Figure S3, Supporting Information). Modeled curves correspond to a carrier lifetime given by the additive recombination rates (or inverse lifetimes) from different origins, i.e.,  $\tau_{\text{avg}}^{-1} = \tau_{\text{SRH}}^{-1} + \tau_{\text{rad}}^{-1} + \tau_{\text{Auger}}^{-1}$ , and calculated based on recombination rate equations for SRH, radiative, and Auger recombination found elsewhere.<sup>[31,32]</sup>

Modeled curves show  $\tau_{\text{avg}}$  remains unchanged at low injection ( $< 3 \times 10^{15} \text{ cm}^{-3}$ ) and reduces proportionally to  $\Delta n^{-2}$  (i.e.,  $\tau_{\text{rad}}$ ) for  $\Delta n > p_0$  as expected from semiconductor device physics. Theoretical trends are similar to the experimental values measured for NaF + RbF samples (filled circles, squares, and triangles). TRPL maps shown in Figure 1 correspond to  $\Delta n \approx 2 \times 10^{15} \text{ cm}^{-3}$  for which  $\tau_{\text{avg}}$  remains almost unchanged (up to 15% deviation) as compared to lower injection according to Figure 5a. Therefore, it is reasonable to assume low injection conditions for the RbF-treated samples. Indeed, low injection condition is most evident for Steel sample whose  $\tau_{\text{avg}}$  remains almost constant for a broader range of  $\Delta n$  (up to  $\approx 10^{16} \text{ cm}^{-3}$ ), consistently with its higher doping concentration estimated from C–V ( $\approx 3 \times 10^{16} \text{ cm}^{-3}$ , see Figure S3, Supporting Information). Higher doping for Steel is attributed to increased Na content (see Figure S4, Supporting Information). Tentatively, concerned to modified effective substrate temperature and modified morphology.

The NaF (cyan asterisks) and No PDT (purple symbols) samples show significant deviations to the model for  $\Delta n > 5 \times 10^{15} \text{ cm}^{-3}$ . The power dependence cannot be explained by SRH and bimolecular recombination for these samples. An alternative explanation could be the presence of specific traps with asymmetry in energy levels and capture/emission rates for electrons and holes, differently as assumed previously.

Another way to infer injection conditions is from the shape of the decays. In principle, in the absence of trapping or strong drift caused by potential fluctuations, low injection conditions generate ideally single exponential decays.<sup>[33]</sup> Our decays at the lowest injection deviate from single exponential behavior (see Figure 5b–f), especially for the NaF sample. A minor transient (from when  $\text{PL} < 0.2$  and  $\text{PL} < 0.05$  for Steel) has been measured. As discussed below, we expect such transients to be related to minor trapping having an irrelevant influence on device performance.<sup>[19]</sup> It is important to mention that the shape of the decays may also be altered by inhomogeneities (as shown in Figure S1, Supporting Information), and by the generation profiles imposed by the bandgap-graded absorber at early times. As illustrated by simulations in Figure S5 of the Supporting Information, graded absorber shows a subtle deviation from single exponential for  $\Delta n < p_0$  injection conditions, turning to a more complicated decay shape at high injection compared to ungraded absorber.

## 2.4. $V_{\text{OC}}$ Loss Analysis from Steady-State PL and TRPL Parameters

Figure 6a shows the distribution of amplitude  $A$ ,  $\tau$  and integrated steady-state PL for all samples analyzed corresponding to the maps depicted in Figure 1. As expected, the three parameters are higher for NaF and NaF + RbF PDTs. The samples

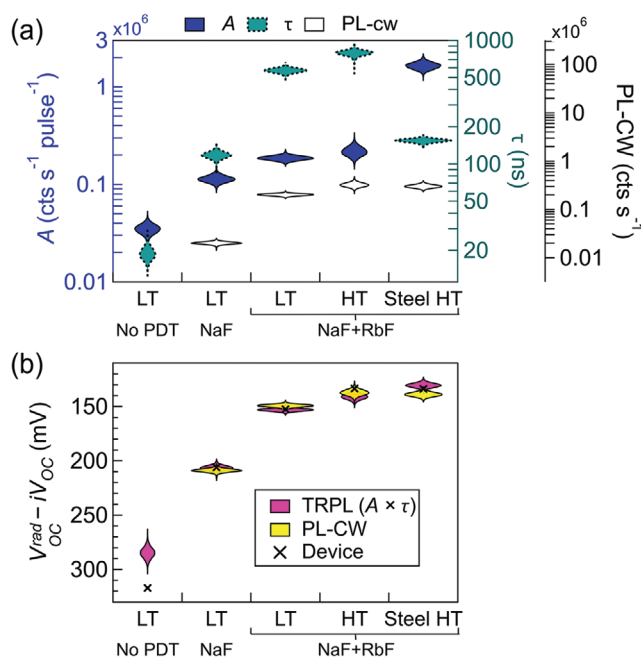


**Figure 6.** Violin plots showing the distribution of a) TRPL parameters  $A$ ,  $\tau$ , and PL-CW calculated from experimental maps of Figure 1, and b)  $V_{\text{OC}}^{\text{rad}} - iV_{\text{OC}}$ , calculated for two different figures of merit: PL-CW and  $A \times \tau$ . Black crosses use terminal  $V_{\text{OC}}$  of the device for the calculation of nonradiative voltage loss. Please note PL-CW axis uses a different scale for better data visualization. Illumination conditions for PL-CW are equivalent to one-sun and comparable to one-sun for TRPL acquisition.

grown at higher temperatures show the highest amplitudes  $A$ , whereas the highest mean lifetimes correspond to Rb-treated grown at LT and HT on SLG. The comparison between high-temperature samples on SLG and Steel is an excellent example of the possibility of decoupling doping concentration and charge carrier lifetime from TRPL parameters. Both samples exhibit similar PL-CW, but five times lower  $\tau$  and approximately seven times higher amplitude  $A$  for Steel.

We now turn to the voltage loss analysis from (TR)PL parameters and the comparison to device  $V_{\text{OC}}$ . From detailed balance, the open-circuit voltage of a solar cell can be expressed as<sup>[34]</sup>

$$V_{\text{OC}} = V_{\text{OC}}^{\text{rad}} + \frac{kT}{q} \ln(Q_e^{\text{LED}}) \quad (1)$$

where  $Q_e^{\text{LED}}$  is the external luminescence quantum efficiency of the solar cell, i.e., the fraction of emitted photons due to radiative recombination that escape out of the solar cell (also referred to as external radiative efficiency<sup>[35,36]</sup>),  $V_{\text{OC}}^{\text{rad}}$  is the open-circuit voltage in the radiative limit (deduced from the experimental EQE curve), i.e.,  $kT/q \ln(J_{\text{sc}}/J_0^{\text{rad}})$  and the other variables have their usual meaning. The second term of Equation (1) is associated with the  $V_{\text{OC}}$  loss due to nonradiative recombination ( $\Delta V_{\text{OC}}^{\text{nonrad}}$ ). Under low injection conditions, and considering equal bimolecular radiative coefficient and that amplitude  $A$  correlates with doping concentration (taken at  $t = 0$ ),  $Q_e^{\text{LED}} \propto A \times \tau$ .<sup>[37]</sup> Hence, an implied open-circuit voltage can be defined as

$$iV_{\text{OC}} = V_{\text{OC}}^{\text{rad}} + \frac{kT}{q} \ln(FoM) + C \quad (2)$$

where FoM corresponds to the figure of merit used for TRPL ( $A \times \tau$ ) or PL-CW, both being relative quantities.  $C$  is an experimentally determined calibration constant dependent on the measurement conditions. To determine the calibration constant and obtain absolute voltages, Equation (2) is employed, in which  $C$  was varied to fit the data  $\Delta V_{OC}^{nonrad}$  versus FoM from several additional devices with different qualities (Figure S6, Supporting Information). Terminal  $V_{OC}$  of Table 1 and  $V_{OC}^{rad}$  are used to obtain  $\Delta V_{OC}^{nonrad}$  (see Section S6, Supporting Information). This assumes  $V_{OC}$  is not modified upon the deposition of ZnO layers and grid to fabricate the devices. We later show this is a reasonable assumption and support it with numerical simulations. A close correlation between terminal  $V_{OC}$  and FoM is observed in Figure S6 of the Supporting Information for devices of various material qualities which supports the use of Equation (2) to estimate the  $iV_{OC}$ . It is important to recall there could be cases for which the determination of  $C$  may no longer be valid. For example, the presence of trapping effects might mask the real properties of the material, being especially important for low to medium quality absorbers. Figure 6b shows a good agreement (disregarding No PDT sample) between the device (black cross) and implied  $\Delta V_{OC}^{nonrad}$  from TRPL and PL-CW. This agreement implies that both TRPL and PL-CW metrics are good approximations to predict  $V_{OC}$  and material quality. On the other hand, TRPL may provide early estimates of the doping concentration of the material. In addition, the voltage loss can also be quantified from doping concentration, and using the lifetime data to determine the minority carrier concentration of the material, as shown elsewhere.<sup>[38,39]</sup> Similar results are obtained using the calibration constant or minority carrier concentrations from lifetime data in most cases (see Section S6, Table S1, Supporting Information), disregarding NaF sample. The disagreement between these two methods in NaF sample is explained by the overestimation of doping concentration from C–V data, as detailed below. Overall, both methods can be used to obtain reasonable estimates of the open-circuit voltage of the devices.

The voltage loss distributions illustrated by the violin plot in Figure 6b lie within a narrow interval for statistical relevance, with maximum mean deviations of 10 and 20 mV for PDT and No PDT samples, respectively. These distributions indicate that

fluctuations of FoMs have a low impact on device  $V_{OC}$  for PDT samples. For absorbers with PDT, predicting  $\Delta V_{OC}^{nonrad}$  by use of TRPL or PL-CW FoMs results in error margins below  $\pm 10$  mV compared to device values. The voltage distribution captures such margins. Only in the case of a low-quality absorber with No PDT, the discrepancy exceeds 30 mV. The distribution tail for TRPL is two times larger than PDT; however, they do not cover the device terminal values.

A comparison with numerical simulations is shown in Figure S7 and Tables S2 and S3 of the Supporting Information, supporting the good  $V_{OC}$  prediction from TRPL parameters for RbF-treated samples. For NaF, numerical simulations and TRPL amplitude suggest about one order of magnitude lower doping concentration than estimated by the C–V technique. This is not surprising because the doping concentration extracted from C–V measurements could be altered by deep and shallow levels, the gradients (e.g., bandgap or doping) in the absorber, interdiffusion, and doping gradients in the absorber/buffer interface, the method of extraction, and, in general, the properties of the heterojunction.<sup>[40–44]</sup> Hence, in many cases, the net doping density calculated from C–V is better conceived as an order of magnitude estimation rather than an accurate value of the real doping within the absorber. Overestimation of the lifetime due to trapping is less likely to occur mainly because we have obtained a very good match between TRPL FoM and terminal  $V_{OC}$  of this device (Figure 6b).

Table 2 shows detailed balance and photovoltaic parameters for all samples. Given the good estimation of implied  $\Delta V_{OC}^{nonrad}$ ,  $Q_e^{LED}$  can also be estimated experimentally according to Equation (2). The highest  $Q_e^{LED}$  is  $\approx 0.6\%$  and  $0.3\%$  for best performing high temperature and low-temperature samples, respectively. For RbF-treated samples, the  $V_{OC}$  is  $\approx 80\%$  of the ideal S–Q limit. The difference between  $V_{OC}^{SQ}$  (calculated with a step-function EQE) and  $V_{OC}^{rad}$  (calculated with experimental EQE) lies between 20 and 30 mV for RbF-treated samples such that any influence of tails or potential fluctuations is in the range of experimental values found for similar samples.<sup>[11]</sup> The lowest  $\Delta V_{OC}^{nonrad}$  is 130 mV and the highest  $Q_e^{LED} \approx 0.6\%$  (Steel), as mentioned previously. Both quantities are in good agreement with the ones calculated by quasi-Fermi level splitting through absolute PL analysis on samples of similar material quality.<sup>[11]</sup>

Among other factors (e.g., nonradiative recombination),  $Q_e^{LED}$  is a parameter dependent on the optical structure. Hence,

**Table 2.** Detailed balance and photovoltaic parameters for all samples analyzed using average quantities from mapping.  $Q_e^{LED}$  and  $\eta_{int}$  are calculated using  $iV_{OC}$  estimated from TRPL FoM. A range is given for  $\eta_{int}$  corresponding to whether band tails absorption was considered or not.  $J_0^{SQ}$  is the detailed balance recombination current calculated from the convolution of the black body radiation and a step-function EQE whereas  $J_0^{rad}$  is the radiative recombination current using the experimental EQE curve.  $E_U$  stands for Urbach energy calculated by fitting the exponential absorption tail in the long wavelength edge of the EQE (fitting range is set to 0.1% and 3% of the EQE long wavelength edge).

Sample	$E_g^{PV}$ [eV]	$E_U$ [meV]	$J_0^{SQ}$ [mA cm <sup>−2</sup> ]	$J_0^{rad}$ [mA cm <sup>−2</sup> ]	$V_{OC}^{SQ}$ [mV]	$V_{OC}^{rad}$ [mV]	$\Delta V_{OC}^{nonrad}$ [mV]	$\eta_{id}$	$Q_e^{LED}$ [%]	$\eta_{int}$ [%]
NaF+RbF Steel (HT)	1.097	13.9	$1.94 \times 10^{-14}$	$3.67 \times 10^{-14}$	855	834	130	1.22	0.65	26 to 33
NaF + RbF SLG (HT)	1.149	16.4	$2.86 \times 10^{-14}$	$6.91 \times 10^{-14}$	903	876	140	1.20	0.44	18 to 23
NaF + RbF SLG (LT)	1.154	15.4	$2.35 \times 10^{-14}$	$4.43 \times 10^{-14}$	908	887	153	1.23	0.27	11 to 17
NaF SLG (LT)	1.168	17.8	$1.45 \times 10^{-14}$	$3.61 \times 10^{-14}$	920	892	207	1.37	0.034	1.5 to 2.6
No PDT SLG (LT)	1.172	19.4	$1.23 \times 10^{-14}$	$4.23 \times 10^{-14}$	924	886	285	–	0.0016	<0.1



optical modeling can be used to assess the fraction of the total recombination that is radiative, which is an excellent metric determining material quality. The internal radiative efficiency ( $\eta_{\text{int}}$ ) evaluates such fraction. From optical modeling,  $\eta_{\text{int}}$  can be calculated as<sup>[35]</sup>

$$\eta_{\text{int}} = \frac{\eta_{\text{ext}}}{\eta_{\text{ext}} \overline{P_{\text{abs}}} + \overline{P_{\text{esc}}}} \quad (3)$$

where  $\eta_{\text{ext}} = Q_{\text{e}}^{\text{LED}}$  and corresponds to the value determined experimentally and shown in Table 2.  $\overline{P_{\text{esc}}}$  and  $\overline{P_{\text{abs}}}$  are approximated through optical modeling, being functions of the geometry, angle, and energy-dependent on the Fresnel coefficients at the front and back of the structure.  $\overline{P_{\text{esc}}}$  is the probability of an emitted photon to escape out of the front of the device whereas  $\overline{P_{\text{abs}}}$  is the probability for an emitted photon to be reabsorbed, averaged over the spontaneous energy distribution and uniformly distributed solid angle of internal emission.<sup>[35]</sup> Hence,  $\eta_{\text{int}}$  is a material quality metric that can be calculated from measurable (TR)PL parameters and optical modeling. With this approach (Equation (3)),  $\eta_{\text{int}}$  can be approximated without prior knowledge of the doping concentration and radiative recombination coefficient of the material.

$\overline{P_{\text{abs}}}$  and  $\overline{P_{\text{esc}}}$  are obtained from previous calculations for CIGS under different scenarios.<sup>[45]</sup> For instance, considering a structure Mo/CIGS/CdS for which CIGS exhibits a band tail absorption  $\approx 15$  meV,  $\overline{P_{\text{abs}}} = 62.8\%$ , and  $\overline{P_{\text{esc}}} = 2.1\%$ . In this case,  $\eta_{\text{int}} \approx 26\%$  for the highest quality sample characterized here. By excluding band tail absorption,  $\overline{P_{\text{abs}}} = 83.5\%$ ,  $\overline{P_{\text{esc}}} = 1.4\%$ , and  $\eta_{\text{int}}$  increases to  $\approx 30\%$ . The high values of  $\overline{P_{\text{abs}}}$  imply a strong photon recycling activity in CIGS even without an optimized back reflector (about 30% back reflectance). However, for photon recycling to be important for  $V_{\text{OC}}$  gain,  $\eta_{\text{int}}$  should be sufficiently high and ideality factors very close or equal to 1 (originating mainly from bulk radiative recombination). Optical ideality factors ( $n_{\text{id}}$ ) were experimentally determined by the slope of PL-CW intensity as a function of the excitation power ( $I$ ), i.e.,  $\text{PL} \propto I^{n_{\text{id}}}$ .<sup>[34]</sup> We measure  $n_{\text{id}}$  between 1.2 and 1.4 for PDT samples around one sun (Figure S8, Supporting Information). Optical ideality factors higher than one have been recently associated to metastable defects whose origin is still under investigation.<sup>[46]</sup> Therefore, despite that about 30% of the recombination is radiative, the voltage loss analysis and optical ideality factors suggest the material is still dominated by nonradiative recombination (in agreement with the results of Figure 4). Optimized back reflectors to maximize the reabsorption probability would provide negligible  $V_{\text{OC}}$  benefits if applied to these structures.

### 3. Conclusions

We have shown PDT homogenizes spatial variations of carrier lifetime and overall PL intensity, with RbF and NaF-treated samples exhibiting lower spatial variations compared to No-PDT. The maximum deviations from the mean in TRPL parameters are within  $\pm 20\%$  and for the No-PDT sample  $\pm 40\%$ . We find no correlation between PL and lifetime maps for PDT samples, and, in general, spatial variations in carrier lifetime

maps are significantly lower than PL-CW. These findings highlight the importance of directly measuring the carrier lifetime to prove spatial variations of the material quality, as this parameter is less sensitive to surface topography than PL-CW. TRPL figure of merit distribution is almost equivalent to the PL-CW figure of merit distribution for RbF-treated samples. For samples exhibiting larger dispersion (No PDT and to a lower extent NaF sample), TRPL detected more significant spatial variations over PL-CW, especially for No PDT sample, which exhibited about  $\pm 40\%$  deviations from mean for TRPL and about  $\pm 20\%$  for PL-CW.

Due to the relatively low (or comparable to bulk) recombination, we could not directly assess GB recombination under wide-field illumination. Nevertheless, the TRPL mapping experiments are sensitive to GB recombination in which PDTs improve the lifetime at grain interiors and grain boundaries. Indeed, the indirect evaluation of GB recombination suggests that GB recombination velocity is diminished upon PDT deposition, being remarkably low for Rb-treated samples ( $< 60 \text{ cm s}^{-1}$ ). Despite this low upper limit of GB recombination velocity, it is not excluded that GB could limit the effective lifetime of the material, thus device performance.

We have used power-dependent TRPL measurements to evaluate the injection conditions and suggested low injection for mapping of high-quality absorbers. The high-quality samples followed the expected transition from SRH to bimolecular recombination. It was more challenging to infer the injection conditions of the material for the low to medium-quality absorbers analyzed here (No PDT and NaF samples). Nevertheless, the comparable voltage losses calculated from continuous-wave, pulsed illumination measurements, and terminal  $V_{\text{OC}}$  confirm the validity of TRPL characterization to predict device performance (PDT samples) and within the limits of investigated samples. For high-quality samples, the carrier lifetime fluctuations have a small impact on device performance ( $< 10 \text{ mV}$ ). We have also shown how TRPL has the additional advantage of decoupling the contributions to the PL signal from doping concentration and lifetime. For NaF-treated absorbers, despite the complex trend of lifetimes with excitation power, TRPL parameters correlate strongly to  $V_{\text{OC}}$ . This correlation and the relatively lower TRPL amplitude measured (as expected from comparison to other samples) suggest that C-V measurements likely overestimate the doping concentration of this material (supported by numerical simulations). Finally, we estimate about 30% of total recombination is radiative for the best samples (with optical ideality factors about 1.2), comparable to state-of-the-art absorbers. Although there is a significant amount of photon recycling, the absorbers are still limited by nonradiative recombination; thus, photon recycling is not expected to yield relevant voltage gain.

### 4. Experimental Section

**Samples Description:** Double bandgap graded CIGS layers were deposited by multistage coevaporation on SLG and stainless-steel substrate with an alkali (or metal) diffusion barrier ( $\text{SiO}_x$ ) before Mo back contact coating in most samples (disregarding sample on SLG grown at high temperature which has no barrier, as described below).

Five samples were grown at two different temperatures (labeled LT at  $\approx 450^\circ\text{C}$  and HT at  $\approx 580^\circ\text{C}$ ). Different alkali PDT were supplied in situ to the CIGS layers, namely: 1) NaF, 2) NaF + RbF with additional RbF supplied at the end of the third stage, i.e., in the so-called (In,Se) capping and 3) No PDT. The solar cells were finished with a chemical bath deposition of CdS (24 minutes for NaF and No-PDT and 14 min for NaF + RbF), RF sputtering of nonintentionally doped ZnO and ZnO:Al, and Ni-Al grids were deposited by e-beam evaporation. No antireflection coating was deposited onto the solar cells. For more information about the sample growth, PDT process, and fabrication of the solar cells, the reader is referred to the work of Nishiwaki and co-workers.<sup>[47,48]</sup>

**Electro-Optical Characterization:** *I*-*V* curves were measured using a four-terminal Keithley 2400 source meter under standard test conditions ( $25^\circ\text{C}$ ,  $1000\text{ W m}^{-2}$ , AM1.5G illumination, ABA-class sun simulator). The *I*-*V* parameters of the solar cells are depicted in Table 2. External Quantum Efficiency was measured using a chopped illumination from a halogen light source, wavelength-selected with a double-grating monochromator. A halogen lamp light bias of about 0.2 sun intensity was applied during the measurements. A certified Si and calibrated Ge solar cells were used for calibration. *C*-*V* profiles were measured with an Agilent E4980ALCR meter at a frequency of 1 kHz. The sample was kept at 300 K. Carrier concentrations were extracted from the apparent doping curve (minimum), assuming an  $n^+p$  junction.

**Bandgap Determination:** For  $V_{\text{OC}}$  loss analysis from TRPL parameters (Section 2.4), Rau et al. procedure was followed.<sup>[34]</sup> The bandgap definition derived by Rau is based on the QE derivative.

**SIMS Measurements:** Compositional depth profiles were measured by SIMS. The primary beam was 25 keV  $\text{Bi}^+$  with a total current of 0.6 pA and a raster size of  $50 \times 50\ \mu\text{m}^2$ . The sputtering beam was 250 nA, 2 keV  $\text{O}_2^+$  with an on-sample area of  $300 \times 300\ \mu\text{m}^2$ . Gallium to Gallium + Indium (GGI) depth profiles were determined by scaling the intensity of elemental traces with integral GGI values obtained from X-ray fluorescence.

**TRPL Mapping:** For TRPL measurements, the finished solar cells with no ARC deposited were etched (5 min in 5% of  $\text{CH}_3\text{CO}_2\text{H}$ ) to remove ZnO:Al and ZnO layers, resulting in a CdS/CIGS/Mo layer structure. As previously shown by Metzger et al.<sup>[18]</sup> and suggested by Weiss et al.,<sup>[19]</sup> the presence of CdS has a minor or null impact on the TRPL decay. The CdS coverage allowed stable optoelectronic response over long periods and access to device parameters for the same absorber where TRPL mapping was performed. For each sample, several maps (>5) have been measured in different locations of the solar cell area, exhibiting similar TRPL parameters and characteristic features.

A MicroTime 100 system coupled to a detection unit from PicoQuant was used for TRPL mapping. The setup comprises an upright microscope and FluoTime 300 unit including detection optics, monochromator, and an InGaAs-based photomultiplier detector (950–1450 nm) from Hamamatsu (H10330A-45). For microscopic mapping, the objective is coupled into a fine piezoscanner with nm-spatial resolution. For photon counting, PicoQuant TCSPC cards in the long-range mode were employed to avoid pile-up effects. A long-range  $20 \times$  objective optimized for the NIR transmission (Olympus LCPLN20XIR) was used with a numerical aperture of 0.45. A detection fiber of 50  $\mu\text{m}$  acting as a pinhole collects the light coming from the objective to the entrance of the monochromator. The optical resolution is  $\approx 2\ \mu\text{m}$ . Wide-field illumination was set by focusing the excitation beam to the objective's back focal plane, and a collimated beam was projected on the sample to achieve low injection conditions. The beam size was about 130  $\mu\text{m}$  ("13.5% metric"), as measured by a NanoScan2 beam profiler. A Laser of 639 nm with <100 ps pulse duration was used as an excitation source with frequencies between 70 kHz and 5 MHz. The excitation was varied in the range of  $1 \times 10^{11}$  to  $2 \times 10^{12}$  photons  $\text{cm}^{-2}$  pulse $^{-1}$  (estimating sample reflectance  $R = 20\%$  for thin CdS and about 10% for thick CdS samples). For the lowest photon density for mapping ( $\approx 3 \times 10^{11}$  photons  $\text{cm}^{-2}$  pulse $^{-1}$ ), the initial injection was  $8 \times 10^{15}$   $\text{cm}^{-3}$  assuming  $\alpha = 6 \times 10^4\ \text{cm}^{-1}$ .<sup>[49]</sup> After few nanoseconds (<10 ns), the carriers redistribute over a region of 1.5  $\mu\text{m}$ . Thus the carrier density reduces to about  $2 \times 10^{15}\ \text{cm}^{-3}$ . Continuous-wave PL maps were also

performed, adjusting the light intensity to obtain the same carrier density calculated for pulsed measurements (using average light intensity). Decays (or continuous wave PL measurements) at each pixel were spectrally integrated.

The lowest count rate for mapping used was higher than 20000 counts  $\text{s}^{-1}$ . Dwell times between 20 and 250 ms per point result in 15–120 min for a map of  $80 \times 80\ \mu\text{m}$  and  $128 \times 128$  pixels. Decays at each pixel were fitted to a single or double exponential employing maximum likelihood algorithms with SymphoTime 2.4 software from PicoQuant.<sup>[50–52]</sup> All fitted parameters with two exponentials are averaged following

$$\tau_{\text{avg}} = \frac{\sum_i A_i \tau_i^2}{\sum_i A_i \tau_i} \text{ where } i \text{ is the number of exponentials. Another definition for average lifetimes is often used, i.e., } \tau_{\text{avg,amp}} = \frac{\sum_i A_i \tau_i}{\sum_i A_i}.$$

The latter formula is more sensitive to the first part of the decay, whereas the former formula is more sensitive to the longest part of the decay. Deviations in the average lifetime below 30% were detected by the use of one or another formula. Such deviations are significant but with minor impact on the trends exhibited in power-dependent measurements and reasonable for  $V_{\text{OC}}$  prediction. For mapping at low injection, a single exponential fit was performed for simplicity (neglecting irrelevant changes in transients at long times) whose values lie roughly between the two average formulas shown before. See Figure S9 of the Supporting Information for the deviations expected for each lifetime formula in all samples. Similar standard deviations were obtained compared to any lifetime distribution, resulting only in magnitude deviations within the range mentioned before (maximum magnitude deviations of 30%).  $\tau$  refers to the effective carrier lifetime from a single exponential fit, and  $\tau_{\text{avg}}$  stands for the effective carrier lifetime calculated from biexponential fit (equation above).

**Drift-Diffusion Simulations:** TCAD simulations were carried out using Sentaurus tool from Synopsys.<sup>[53]</sup> 1D simulations are used for *I*-*V* and TRPL simulations (without GB recombination). *I*-*V* simulations implement ohmic boundary conditions at both contacts. For TRPL, zero current at the contacts was set to emulate open-circuit conditions. Front and back surface recombination velocities were neglected. Carriers are expected to drift and diffuse to the so-called notch faster than 10 ns, and recombination at surfaces is inhibited due to the front bandgap grading (+ CdS layer),<sup>[19]</sup> and the back bandgap grading.<sup>[25]</sup> Therefore, the overall decay was expected to be dominated by the notch properties. A pulse of some tenths of ps (640 nm wavelength) was implemented with energy corresponding to the one used in the experiments. The CIGS absorber bandgap grading was modeled with the corresponding absorption coefficient dependence<sup>[49]</sup> based on the GGI depth profile obtained from XRF-calibrated SIMS measurements (see Figure S10, Supporting Information). More details and material parameters can be found elsewhere.<sup>[45]</sup>

TRPL simulations were performed on a 200  $\mu\text{m}$  length structure with 1  $\mu\text{m}$  absorber thickness (no bandgap grading included) to evaluate GB recombination. A centered boundary condition was set to emulate different grain boundary recombination velocities. The illumination source was a Gaussian beam of 640 nm and 130  $\mu\text{m}$  width centered at the GB. TRPL curves were extracted by integrating the radiative recombination over columnar regions of different lengths (e.g., optical resolution) centered at the GB.

## Supporting Information

Supporting Information is available from the Wiley Online Library or from the author.

## Acknowledgements

This work received financial support in part from the Swiss State Secretary for Education, Research and Innovation (SERI) under Contract

No. 17.00105 (EMPIR project HyMet) and from the Swiss Federal Office of Energy (SFOE) (SI/501614-01 "ImproCIS"). The EMPIR programme was cofinanced by the Participating States and by the European Union's Horizon 2020 research and innovation programme.

Open access funding provided by ETH-Bereich Forschungsanstalten.

## Conflict of Interest

The authors declare no conflict of interest.

## Data Availability Statement

The data that support the findings of this study are available from the corresponding author upon reasonable request.

## Keywords

charge carrier lifetime, CIGS, mapping, open-circuit voltage, radiative efficiency, time-resolved photoluminescence

Received: September 8, 2021

Revised: November 22, 2021

Published online: December 15, 2021

- [1] A. Delamarre, L. Lombez, J.-F. Guillemoles, *J. Photonics Energy* **2012**, 2, 027004.
- [2] K. Bothe, G. H. Bauer, T. Unold, *Thin Solid Films* **2002**, 403, 453.
- [3] A. Nikolaeva, M. Krause, J. Marquez, C. Hages, S. Levchenko, T. Unold, W. Witte, D. Hariskos, D. Abou-Ras, *2018 IEEE 7th World Conf. on Photovoltaics Energy Conversion (A Joint Conf. of 45th IEEE PVSC, 28th PVSEC and 34th EU PVSEC)*, IEEE, Piscataway, NJ **2018**, p. 2512.
- [4] A. Redinger, S. Kretschmar, T. Unold, *IEEE 43rd Photovoltaics Spec. Conf.* **2016**, 2016, 3559.
- [5] A. Delamarre, M. Paire, J. F. Guillemoles, L. Lombez, *Prog. Photovoltaics Res. Appl.* **2015**, 23, 1305.
- [6] S. Johnston, T. Unold, I. Repins, R. Sundaramoorthy, K. M. Jones, B. To, N. Call, R. Ahrenkiel, *J. Vac. Sci. Technol., A* **2010**, 28, 665.
- [7] G. El-Hajje, D. Ory, J.-F. Guillemoles, L. Lombez, *Appl. Phys. Lett.* **2016**, 109, 022104.
- [8] H. Guthrey, J. Moseley, J. Nishinaga, H. Shibata, H. Takahashi, M. Al-Jassim, *IEEE J. Photovoltaics* **2018**, 8, 1833.
- [9] N. Nicoara, R. Manaligod, P. Jackson, D. Hariskos, W. Witte, G. Sozzi, R. Menozzi, S. Sadewasser, *Nat. Commun.* **2019**, 10, 3980.
- [10] M. Kawamura, T. Yamada, N. Suyama, A. Yamada, M. Konagai, *Jpn. J. Appl. Phys.* **2010**, 49, 0623011.
- [11] M. Krause, A. Nikolaeva, M. Maiberg, P. Jackson, D. Hariskos, W. Witte, J. A. Márquez, S. Levchenko, T. Unold, R. Scheer, D. Abou-Ras, *Nat. Commun.* **2020**, 11, 4189.
- [12] M. Raghuvanshi, R. Wuerz, O. Cojocaru-Mirédin, *Adv. Funct. Mater.* **2020**, 30, 2001046.
- [13] D. Abou-Ras, B. Schaffer, M. Schaffer, S. S. Schmidt, R. Caballero, T. Unold, *Phys. Rev. Lett.* **2012**, 108, 075502.
- [14] S. Johnston, T. Unold, I. Repins, A. Kanevce, K. Zaunbrecher, F. Yan, J. V. Li, P. Dippo, R. Sundaramoorthy, K. M. Jones, B. To, *J. Vac. Sci. Technol., A* **2012**, 30, 04D111.
- [15] D. Kuciauskas, D. Lu, S. Grover, G. Xiong, M. Gloeckler, *Appl. Phys. Lett.* **2017**, 111, 233902.
- [16] D. Kuciauskas, T. H. Myers, T. M. Barnes, S. A. Jensen, A. Motz, *Appl. Phys. Lett.* **2017**, 110, 083905.
- [17] C. Kraft, H. Hempel, V. Buschmann, T. Siebert, C. Heisler, W. Wesch, C. Ronning, *J. Appl. Phys.* **2013**, 113, 124510.
- [18] W. K. Metzger, I. L. Repins, M. A. Contreras, *Appl. Phys. Lett.* **2008**, 93, 022110.
- [19] T. P. Weiss, R. Carron, M. H. Wolter, J. Löckinger, E. Avancini, S. Siebentritt, S. Buecheler, A. N. Tiwari, *Sci. Technol. Adv. Mater.* **2019**, 20, 313.
- [20] W. K. Metzger, *Sol. Energy Mater. Sol. Cells* **2008**, 92, 1123.
- [21] M. Ochoa, S. Nishiwaki, S.-C. Yang, A. N. Tiwari, R. Carron, *Phys. Status Solidi RRL* **2021**, 15, 2100313.
- [22] A. Kanevce, D. Kuciauskas, D. H. Levi, A. M. Allende Motz, S. W. Johnston, *J. Appl. Phys.* **2015**, 118, 045709.
- [23] R. K. Ahrenkiel, S. W. Johnston, *Sol. Energy Mater. Sol. Cells* **2009**, 93, 645.
- [24] M. A. Contreras, J. Tuttle, A. Gabor, A. Tennant, K. Ramanathan, S. Asher, A. Franz, J. Keane, L. Wang, J. Scofield, R. Noufi, *1st World Conference on Photovoltaic Energy Conversion - WCPEC (A Joint Conference of PVSC, PVSEC and PSEC)*, IEEE, Piscataway, NJ **1994**, p. 68.
- [25] T. Feurer, B. Bissig, T. P. Weiss, R. Carron, E. Avancini, J. Löckinger, S. Buecheler, A. N. Tiwari, *Sci. Technol. Adv. Mater.* **2018**, 19, 263.
- [26] C. Persson, A. Zunger, *Appl. Phys. Lett.* **2005**, 87, 211904.
- [27] G. W. 't Hooft, C. van Oordorp, *J. Appl. Phys.* **1986**, 60, 1065.
- [28] L. Chen, J. Lee, W. N. Shafarman, *IEEE J. Photovoltaics* **2014**, 4, 447.
- [29] S.-C. Yang, J. Sastre, M. Krause, X. Sun, R. Hertwig, M. Ochoa, N. Tiwari, A. R. Carron, *Sol. RRL* **2021**, 5, 2100108.
- [30] R. Scheer, H. W. Schock, *Chalcogenide Photovoltaics: Physics, Technologies, and Thin Film Devices*, Wiley-VCH, Weinheim, Germany **2011**.
- [31] K. Dieter, *Schroder Semiconductor Material and Device Characterization*, IEEE Press, Piscataway, NJ **2006**.
- [32] T. Kirchartz, J. A. Márquez, M. Stollerfoht, T. Unold, *Adv. Energy Mater.* **2020**, 10, 1904134.
- [33] M. Maiberg, F. Bertram, M. Müller, R. Scheer, *J. Appl. Phys.* **2017**, 121, 085703.
- [34] U. Rau, B. Blank, T. C. M. Müller, T. Kirchartz, *Phys. Rev. Appl.* **2017**, 7, 044016.
- [35] M. A. Steiner, J. F. Geisz, I. García, D. J. Friedman, A. Duda, S. R. Kurtz, *J. Appl. Phys.* **2013**, 113, 123109.
- [36] M. A. Green, A. W. Y. Ho-Baillie, *ACS Energy Lett.* **2019**, 4, 1639.
- [37] R. J. Nelson, R. G. Sobers, *J. Appl. Phys.* **1978**, 49, 6103.
- [38] D. Kuciauskas, J. Moseley, C. Lee, *Sol. RRL* **2021**, 5, 2000775.
- [39] M. Stollerfoht, C. M. Wolff, J. A. Márquez, S. Zhang, C. J. Hages, D. Rothhardt, S. Albrecht, P. L. Burn, P. Meredith, T. Unold, D. Neher, *Nat. Energy* **2018**, 3, 847.
- [40] F. Werner, F. Babbe, H. Elanzeery, S. Siebentritt, *Prog. Photovoltaics Res. Appl.* **2019**, 27, 1045.
- [41] S. P. Harvey, S. Johnston, G. Teeter, *IEEE 44th Photovoltaics Specialists Conf. PVSC, IEEE, Piscataway, NJ* **2017** p. 2414.
- [42] M. Cwil, M. Igalson, P. Zabierowski, S. Siebentritt, *J. Appl. Phys.* **2008**, 103, 063701.
- [43] G. Sozzi, M. Lazzarini, R. Menozzi, R. Carron, E. Avancini, B. Bissig, S. Buecheler, A. N. Tiwari, *Conf. Record of the IEEE Photovoltaic Specialists Conf.*, IEEE, Piscataway, NJ **2016**, p. 2283.
- [44] F. Werner, F. Babbe, J. Burkhart, C. Spindler, H. Elanzeery, S. Siebentritt, *ACS Appl. Mater. Interfaces* **2018**, 10, 28553.
- [45] M. Ochoa, S. Buecheler, A. N. Tiwari, R. Carron, *Energy Environ. Sci.* **2020**, 13, 2047.
- [46] T. P. Weiss, F. Ehre, V. Serrano-Escalante, T. Wang, S. Siebentritt, *Sol. RRL* **2021**, 5, 2100063.
- [47] S. Nishiwaki, T. Feurer, B. Bissig, E. Avancini, R. Carron, A. N. Tiwari, *Thin Solid Films* **2017**, 633, 18.



- [48] R. Carron, S. Nishiwaki, T. Feurer, R. Hertwig, E. Avancini, J. Löckinger, S. C. Yang, S. Buecheler, A. N. Tiwari, *Adv. Energy Mater.* **2019**, 9, 1900408.
- [49] R. Carron, E. Avancini, T. Feurer, B. Bissig, P. A. Losio, R. Figi, C. Schreiner, M. Bürki, E. Bourgeois, Z. Remes, M. Nesladek, S. Buecheler, A. N. Tiwari, *Sci. Technol. Adv. Mater.* **2018**, 19, 396.
- [50] M. Wahl, F. Koberling, M. Patting, E. H. Rahn, *Curr. Pharm. Biotechnol.* **2004**, 5, 299.
- [51] K. Santra, J. Zhan, X. Song, E. A. Smith, N. Vaswani, J. W. Petrich, *J. Phys. Chem. B* **2016**, 120, 2484.
- [52] J. Enderlein, R. Erdmann, *Opt. Commun.* **1997**, 134, 371.
- [53] Synopsys Sentaurus Device User Guide. version P-2019.3, **2019**.